JANUARY 28 2026

Time-dependent size stability and shell behaviors of lipid-coated microbubbles

Saikat Halder ; Mehmet Yapar ; Sanku Mallik ; Kausik Sarkar

J. Acoust. Soc. Am. 159, 850–861 (2026)
https://doi.org/10.1121/10.0042248

JASA ARTICLE

Time-dependent size stability and shell behaviors of lipid-coated microbubbles

Saikat Halder,[1] Mehmet Yapar,[1] Sanku Mallik,[2] and Kausik Sarkar[1,a)]
[1]Department of Mechanical and Aerospace Engineering, The George Washington University, Washington, DC 20052, USA
[2]College of Pharmacy and Allied Health Professions, South Dakota State University, Brookings, South Dakota 57007, USA

ABSTRACT:
Microbubbles are excellent contrast-enhancing agents for ultrasound imaging. A long shelf life with a robust size distribution is critical for their efficacy. Here, we investigated the long-term stability and attenuation of a custom-made polydisperse microbubble suspension. The microbubbles were prepared using mechanical agitation with a gas core of perfluorobutane (C_4F_{10}), and a 9:1 molar ratio mixture of 1,2-dipalmitoyl-sn-glycero-3-phosphatidylcholine (DPPC) and 1,2-dipalmitoyl-sn-glycero3-phosphatidylethanolamine-polyethyleneglycol-2000 (DPPE-PEG2000) lipids. Their size distribution and attenuation response were measured in regular intervals over 30 days. The size remained the same (∼2.25 μm) for the first 13 days before slightly increasing to ∼2.5 μm. The microbubble concentration decreased with time ($7.14 \pm 1.12 \times 10^9$ MB/mL initially and $3.29 \pm 0.66 \times 10^9$ MB/mL at day 30), resulting in a corresponding decrease in attenuation. We determined the shell properties of microbubbles by applying the exponential elasticity model (EEM) to the attenuation. Like the size, the shell elasticity and viscosity remained unchanged for 13 days and then increased by ∼50% and ∼200%, respectively. The study sheds light on the shelf life and *in vitro* stability of lipid-coated microbubbles, offering valuable information about their effectiveness as ultrasound contrast agents. https://doi.org/10.1121/10.0042248
(Received 4 September 2025; revised 29 December 2025; accepted 30 December 2025; published online 28 January 2026)
[Editor: Charles C. Church] Pages: 850–861

INTRODUCTION

Microbubbles are contrast agents for ultrasound imaging with a diameter of 1–10 μm (Paul *et al.*, 2014; Versluis *et al.*, 2020; Sarkar, 2025). They significantly enhance the image contrast due to their high scattering cross sections resulting from the strong mismatch in acoustic impedance with the surrounding tissues and fluids. They are filled with low-soluble gases, such as sulfur hexafluoride (SF_6) and perfluorocarbons (PFCs), and are encapsulated with a nanometer-thick protective shell of lipids, proteins, and polymers (Cosgrove, 2006; Frinking *et al.*, 2020; Stride *et al.*, 2020). Microbubbles are also potential candidates for other biomedical applications, such as drug delivery (Ferrara *et al.*, 2007; Qin *et al.*, 2009; Eisenbrey and Forsberg, 2010; Fix *et al.*, 2015), gene and tumor therapy (Wu and Li, 2017; Zhu *et al.*, 2024; Halder *et al.*, 2025), and subharmonic aided pressure estimation (SHAPE) (Forsberg *et al.*, 2005; Eisenbrey *et al.*, 2015; Dave *et al.*, 2017; Gupta *et al.*, 2019; Gupta *et al.*, 2021; Esposito *et al.*, 2023; Azami *et al.*, 2024). The stability and sustained acoustic performance of a microbubble agent are critical to its efficacy in any of its target applications. Here, we investigated the long-term stability and acoustic responses (over a 30 day period) of a laboratory-made polydisperse microbubble suspension.

Microbubble responses to an acoustic wave are dependent on its resonance frequency, which, in turn, is determined by the size of the microbubbles and their shell properties (Chatterjee and Sarkar, 2003; Sarkar *et al.*, 2005; Paul *et al.*, 2010; Segers *et al.*, 2016a). There are several commercial ultrasound contrast agents available with different formulations and shelf lives after activation using the procedure specified by the manufacturer (listed in Table I).

Microbubble dissolution results from gas diffusion, coalescence, and shell degradation. We have previously modeled the dissolution of microbubbles (Katiyar *et al.*, 2009; Sarkar *et al.*, 2009; Katiyar and Sarkar, 2010) and showed that an encapsulated microbubble initially increases its radius due to dissolved air rushing in and later decreases due to the PFC leaving the bubble (also see Kwan and Borden, 2010). The process is driven by the effective residual surface tension of the encapsulation shell, the saturation level of the surrounding medium, and most importantly, the permeability of the gases through the shell. Assuming a finite nonzero permeability leads to a dissolution time that varies from a few seconds to several hours. Experimentally, Xu *et al.* (2008) compared two different methods for microbubble preparation: several minutes of mechanical agitation and sonication. They found that the diameter of microbubbles prepared by the first method remained the same over time, while the ones prepared by the second method changed significantly within 1 min of preparation. Feshitan *et al.* (2009) successfully isolated 1–2 and 4–5 μm microbubbles from lipid-coated perfluorobutane-filled microbubbles using centrifugation and showed that the isolated microbubbles were stable over 2 days. Conversano *et al.* (2010) studied the

a)Email: sarkar@gwu.edu

https://doi.org/10.1121/10.0042248

TABLE I. Ultrasound contrast agents and their gas, shell, and shelf life after activation. DPPC: 1,2-dipalmitoyl-sn-glycero-3-phosphatidylcholine; DPPA: 1,2-Dipalmitoyl-sn-glycero-3-phosphate DPPE-MPEG5000: N-(Carbamoyl-methoxypolyethylene glycol 5000)-1,2-dipalmitoyl-sn-glycero-3-phosphoethanolamine; DSPC: 1,2-distearoyl-sn-glycero-3phosphocholine; DPPG-Na: 1,2-Dipalmitoyl-sn-glycero-3-phosphoglycerol, sodium salt.

Ultrasound contrast agents	Manufacturer	Gas	Shell	Shelf life (h)
Optison (Optison, 1998)	(GE Healthcare, 1998)	Perflutren (C_3F_8)	Denatured human albumin	12
Definity/Luminity (Definity, 2001)	(Lantheus, 2001/2006)	Perflutren (C_3F_8)	DPPC, DPPA, DPPE-MPEG5000	12
Lumason/SonoVue (Lumason, 2001)	(Bracco, 2001/2014)	Sulfur hexafluoride (SF_6)	DSPC, DPPG-Na, palmitic acid	3
Sonazoid (Sonazoid, 2006)	(GE Healthcare, 2006)	Perfluorobutane (C_4F_{10})	Hydrogenated egg yolk phosphatidyl serine (HEPS)	2

dissolution behavior of BR14, a phospholipid-shelled microbubble, based on time-scheduled size distribution measurements. They showed that there was an initial transient diameter growth due to the ingression of air into the microbubbles and slower diffusion out of perfluorobutane from the microbubbles. Recently, Pouliopoulos *et al.* (2020) studied the temporal stability of lipid-shelled microbubbles over 21 days, but sampling at an interval of 7 days, to find that the mean radius over four data points did not change. However, the concentration continually decreased. They obtained an exponential fit with a decay constant of 0.02 day^{-1}. These past studies underscore the need for further long-time study of microbubble stability and their behaviors.

Microbubble behaviors—their stability as well as ultrasound response—depend on the stabilizing encapsulating shell made of lipids, proteins, and other surface-active molecules. There have been many models of bubble encapsulation, starting with the pioneering works of de Jong *et al.* (1992)—an empirical model—and that of Church, who modeled the shell as a finite layer of linear viscoelastic solid (Church, 1995; Hoff *et al.*, 2000). Because of the monomolecular nature of the shell, our group proposed a zero-thickness interfacial rheological model with a constant surface tension and an interfacial viscosity term—the Newtonian model (NM) (Chatterjee and Sarkar, 2003). Over the years, interfacial rheology has become the standard approach for shell modeling. We subsequently improved/modified the NM model, guided by experiments and physical considerations (Sarkar, 2025), first to a linear viscoelastic model [constant elasticity model (CEM)] with an interfacial elasticity (Sarkar *et al.*, 2005) and later to a nonlinear strain-softening model [exponential elasticity model (EEM)] (Paul *et al.*, 2010). Marmottant *et al.* (2005) proposed a model identical to CEM, but with a critical additional component that the shell is elastic only above a shell buckling radius and below a shell breakup radius, which proved critical for explaining experimental observations, such as "compression-only behaviors" (de Jong *et al.*, 2007). Applying them to experiments, we have shown that the EEM and Marmottant models (MM) offer very similar characteristic properties (Paul *et al.*, 2013; Kumar and Sarkar, 2015, 2016; Azami *et al.*, 2022). There have been other theoretical efforts introducing shear-dependent interfacial shell viscosity (Doinikov *et al.*, 2009), more generalized surface continuum mechanics models (Dash and Tamadapu, 2022b,a), and effects of compressibility and anisotropy in a finite-thickness linear viscoelastic solid (Chabouh *et al.*, 2021).

Here, we investigated the variation in microbubble mean size, total concentration, and attenuation characteristics of a laboratory-made lipid-coated polydisperse microbubble suspension with a C_4F_{10} gas core over a 30 day period. Additionally, we estimated the shell properties over time using the EEM developed in our laboratory (Paul *et al.*, 2010; Paul *et al.*, 2013), which, as noted above, has proved adequate for characterizing the changing microbubble behaviors over the 30 day period. We also computed the MM model, in addition to the EEM model for the shell properties estimation. The goal of this study is to investigate the long-time stability of microbubbles and characterize their changing material properties. Both affect microbubble echogenicity and their effective clinical applications. We have been using microbubbles only within 3–6 h after production, leading to discarding 80% of the typical vial volume. This practice conforms with typical commercial microbubbles listing less than 2–12 h of shelf lives (see Table I). The stability study undertaken here is also aimed at eliminating this wasteful restriction.

METHODS

Microbubble preparation and characterization

Microbubbles were produced using the mechanical agitation method, which has been summarized extensively elsewhere (Xu *et al.*, 2008; Azami *et al.*, 2022; Azami *et al.*, 2023). The gas core of perfluorobutane (PFB or C_4F_{10}) (FluoroMed L.P., Round Rock, TX), protected with lipid shells of 1,2-dipalmitoyl-sn-glycero-3-phosphatidylcholine (DPPC) and 1,2-dipalmitoyl-sn-glycero3-phosphatidylethanolamine-polyethyleneglycol-2000 (DPPE-PEG2000) (Avanti Polar Lipids, Alabaster, AL), was used to create the laboratory-made microbubbles. The lipid shells were a 9:1 molar ratio mixture of DPPC and DPPE-PEG2000. First, 7 mg of DPPC powder and 3 mg of DPPE-PEG2000 powder were mixed in 1.5 mL of propylene glycol, and the mixture was kept inside a heated circulating water bath (MX15H135-V11B, VWR International, Bridgeport, NJ) at 53 °C for 20 min. After attaining a clear solution, a mixture of 8 mL of phosphate-buffered saline (PBS) and 0.5 mL of glycerol was added. The final mixture of 1 mg/mL lipid solution was kept inside the hot water bath for another 60 min at 53 °C with a gentle stir for 1 min every 10 min. The solution was allowed to cool

down at room temperature for 30 min and then stored at 4 °C for future use. Microbubbles were prepared by injecting 1.5 mL of the lipid solution into a 2 mL glass vial (Med Lab Supply, Pompano Beach, FL). Then, the vial was sealed with a rubber head (Med Lab Supply, Pompano Beach, FL) and clamped with a metal cap (Med Lab Supply, Pompano Beach, FL). PFB gas was injected at 60 kPa gauge pressure inside the vial after removing the header space air. The lipid–gas mixture was agitated by a vial mixer (VIALMIX, Lantheus, Billerica, MA) for 45 s, producing a milky white microbubble solution. The prepared microbubbles were allowed to stabilize at 4 °C for 15 min before the experiments.

The size and total concentration were measured for the characterization of the microbubbles using an optical microscopy method (Sennoga *et al.*, 2010; Sennoga *et al.*, 2012). 10 μL of 200× diluted microbubble solution in de-ionized (DI) water was inserted into a hemocytometer counting chamber (model 15170-208, VWR, Swedesboro, NJ) for capturing the images using a 20-megapixel complementary metal-oxide-semiconductor (CMOS) camera (MU2003-BI, Amscope, Irvine, CA) connected to an inverted optical microscope (IN480TC-20MBI3, Amscope, Irvine, CA) at 40× magnification. Twelve images containing microbubbles were acquired at random places across the counting chamber. A background image was also taken to remove the uncertainties in counting the microbubbles properly. The images were then processed using the MATLAB software (The MathWorks, Natick, MA) for counting and measuring the size distribution of microbubbles. First, the background image was subtracted from the microbubble image. Then, the modified image was converted to a binary image by using a maximum entropy threshold process. The thresholding was calculated using a MATLAB function that divides the image into two regions: foreground and background by determining the optimal threshold value that maximizes the entropy between the two regions (Gargouri, 2025). After that, the areas of each microbubble were measured and recorded by analyzing the particles. Finally, the area data were used to calculate the mean size and the size distribution. This processing was repeated at least three times for each batch of lipid solution. With the numerical aperture of the microscope's objective lens, $NA = 0.65$ (manufacturer's note), wavelength $\lambda = 700$ nm (yellow halogen lamp; Ogien and Dubois, 2016), the optical resolution limit of the microscope is $d = \lambda/2NA = 0.54$ μm (Abbe, 1873, 1882; Fukutake, 2020). Therefore, microbubbles smaller than 0.6 μm were neglected using the range of 0.6–10 μm for all the size distribution analysis. Also, note that smaller microbubbles contributed very little at typical frequencies for diagnostic applications (Gorce *et al.*, 2000). Using size ranges of 0.5–10 μm and 0.8–10 μm led to minimal changes in mean size (<2%), total concentration (<3%), and total volume concentration (<0.2%), as well as in interfacial properties (<0.5%).

Attenuation measurement

The attenuation due to microbubbles was measured using a custom-made acrylic setup (Azami *et al.*, 2022; Azami *et al.*, 2025), which can be seen in Fig. 1. An acrylic container was filled with 140 mL of DI water for measuring the control signals. After that, 350 μL of 400× diluted microbubble suspensions were added to the same acrylic container to measure the microbubble signals. The final dilution was 1:160000 for all the attenuation experiments. The dilution is similar to the one used previously by our group (Sarkar *et al.*, 2005) and was chosen to offer a strong signal; it also aligns well with clinical dosages for contrast-enhanced ultrasound reported in the literature (Forsberg *et al.*, 2007; Halldorsdottir *et al.*, 2011; Eisenbrey *et al.*, 2013; Gupta *et al.*, 2019; Nio *et al.*, 2020). The suspension was continuously stirred with a relatively low speed (60 rpm) using a magnetic stirrer (model 403N0105, Fisher Scientific, Pittsburgh, PA) inside the container to ensure homogeneity without any microbubble disruption. A pulser–receiver (model 5800, Panametrics, Olympus, Waltham, MA) in pulse-echo mode was used to transmit a broadband signal through a 5 MHz (–6 dB bandwidth: 3.28–6.33 MHz) single-element flat transducer (V309, Olympus, Waltham, MA) with a pulse repetition frequency (PRF) of 100 Hz. The same pulser–receiver was used to receive the

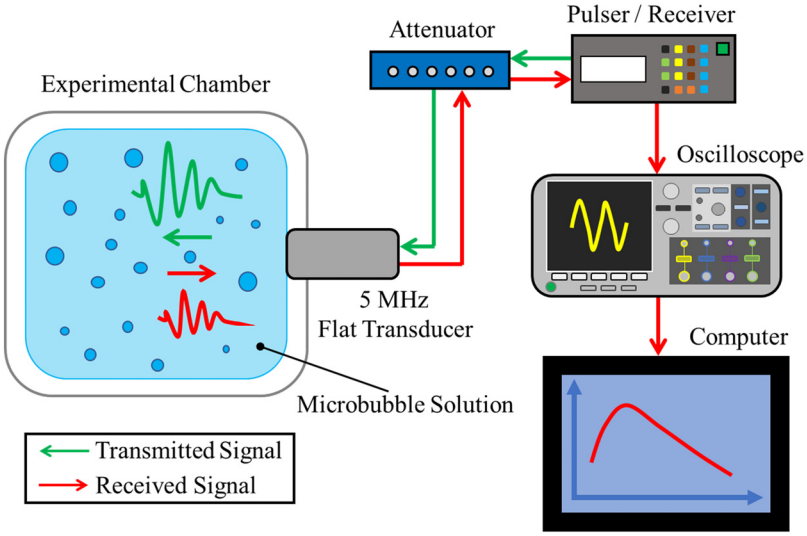

FIG. 1. Experimental setup for measuring attenuation from microbubble solution.

https://doi.org/10.1121/10.0042248

signal reflected from the back wall of the experimental chamber with a 20 dB amplification. An external attenuator (432D, Kay Elements Corporation, Pine Brook, NJ) with an 11 dB dampening was used to ensure that the signal is sufficiently small, appropriate for the linear theory assumption. The received signal was then fed into an oscilloscope (MDO 3024, Tektronix, Beaverton, OR) with a delay of 73 μs and a sampling rate of 1.25 GHz. A MATLAB program was used to record 20 time-voltage signals in 64 sequence average mode before and after microbubble injection inside the experimental chamber. The attenuation was calculated by using the fast Fourier transform (FFT) of the signals without (control) and with microbubbles as follows:

$$\alpha(\omega) = \frac{10}{d}\log\left(\frac{V^2_{control}(\omega)}{V^2_{microbubble}(\omega)}\right), \tag{1}$$

where $\alpha(\omega)$ is the attenuation coefficient in dB/cm, d is the distance between the chamber back wall and flat transducer face, and $V_{control}$ and $V_{microbubble}$ are the recorded signals without and with microbubbles. All the attenuation experiments were repeated at least six times for each batch of lipid solution.

Modeling shell properties

A Rayleigh–Plesset (RP) type equation for an incompressible flow is used to describe the encapsulated microbubble dynamics. The EEM, proposed by our group (Paul *et al.*, 2010; Paul *et al.*, 2013), is introduced to the RP equation for estimating the shell properties (elasticity, viscosity, and surface tension). It offers an interfacial model of the shell with a nonlinear strain-softening elasticity (Sarkar *et al.*, 2005). Various popular shell models have been shown to follow a common interfacial framework (Katiyar and Sarkar, 2011). Note that recently, we have shown that the EEM model predicts nearly identical shell properties for a microbubble made in our laboratory as the popular MM model (Azami *et al.*, 2022). The modified RP equation is as follows:

$$\begin{aligned}\rho\left(R\ddot{R}+\frac{3}{2}\dot{R}^2\right) &= P_{G0}\left(\frac{R_0}{R}\right)^{3k}\left(1-3k\frac{\dot{R}}{c}\right)-\frac{4\mu\dot{R}}{R}\\ &\quad -\frac{4\kappa^S\dot{R}}{R^2}-\frac{2\gamma(R)}{R}-P_0+P_A\sin\omega t,\\ \gamma(R) &= \gamma_0+E^S\beta,\ \ E^S=E^S_0\exp\left(-\alpha^S\beta\right)\ \text{when}>0\\ &\quad \text{otherwise}=0,\ \ \beta=\left(\frac{R}{R_E}\right)^2-1,\end{aligned} \tag{2}$$

where ρ is the density of the fluid, R is the time-dependent radius of the microbubble, R_0 is the initial radius of the microbubble, R_E is the unstrained radius of the microbubble, P_{G0} is the microbubble's initial gas core pressure, k is the polytropic constant of the gas, c is the sound speed inside the media, μ is the fluid viscosity, κ^S is the shell viscosity of the microbubble, γ is the effective surface tension, P_0 is the ambient pressure, P_A is the acoustic pressure amplitude of the sinusoidal excitation, ω is the angular frequency for the ultrasonic excitation, γ_0 is the surface tension corresponding to unstrained radius, E^S is the shell elasticity of the microbubble, E^S_0 is the shell elasticity at the reference level of unstrained radius, and α^S is the EEM model parameter. The modified RP equation [Eq. (2)] is linearized by assuming a periodic excitation with sufficiently low amplitude for obtaining a simple harmonic oscillator. From the oscillator, the resonance frequency ω_0 and the damping term δ can be obtained for EEM. The resonance frequency and the damping term are as follows:

$$\begin{aligned}\omega_0^2 &= \frac{1}{\rho R_0^2}\left[3kP_0+\frac{2E^S_0}{R_0}\left(\frac{\eta}{\alpha^S}\right)\left(1+2\alpha^S-\eta\right)\right],\\ \eta &= \sqrt{1+\frac{4\gamma_0\alpha^S}{E^S_0}},\end{aligned} \tag{3}$$

$$\delta = \frac{1}{\rho\omega_0 R_0^2}\left(4\mu+\frac{4\kappa^S}{R_0}+\frac{3kP_{G0}R_0}{c}\right). \tag{4}$$

The extinction cross section σ_e of a microbubble with an initial radius of R_0 is given by

$$\sigma_e = 4\pi R_0^2\frac{c\delta}{\omega_0 R_0}\frac{\Omega^2}{\left[\left(1-\Omega^2\right)^2+\Omega^2\delta^2\right]},\quad \Omega=\frac{\omega_0}{\omega}. \tag{5}$$

The attenuation through a microbubble suspension is obtained by integrating the extinction cross section over the whole microbubble size distribution:

$$\alpha(\omega) = 10\log^e_{10}\int_{R_{\min}}^{R_{\max}}\sigma_e(R\,;\,\omega)n(R)dR. \tag{6}$$

Here, e is the natural logarithm base, and $n(R)dR$ is the number of microbubbles per unit volume with a radius between R and $R+dR$. The integral can be evaluated in the range of microbubble radii (R_{min}, R_{max}) by using the microbubble properties and size distribution. The attenuation values obtained from the experiment [Eq. (1)] and the EEM model [Eq. (6)] were used to formulate a sum of squared error (SSE) function

$$Er\left(E^S_0,\kappa^S,\gamma_0,\alpha^S\right) = \sum_{i=1}^{n}\left[\alpha^{EEM}(\omega_i)-\alpha^{\text{Exp}}(\omega_i)\right]^2. \tag{7}$$

It was minimized using MATLAB to estimate the shell properties E^S_0, κ^S, γ_0 and α^S. The confidence interval for all properties is calculated by varying the properties' values one by one until the SSE is doubled.

Experimental procedure

Experiments were performed over a 30 day period to understand the stability of the microbubbles under different acoustic excitations. The experiments were conducted on different days, i.e., D0T0 (Day 0 initial time), D0T6 (Day 0 6th hour), D1 (1st day), D2 (2nd day), D3 (3rd day), D4 (4th day), D7 (7th day), D10 (10th day), D13 (13th day), D20 (20th day), and D30 (30th day), respectively. The progressively larger intervals of recording are dictated by the amount

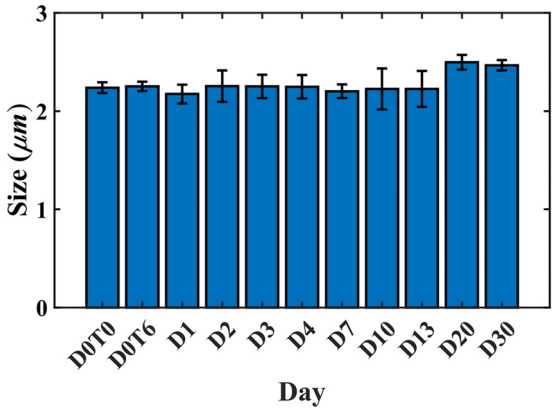

FIG. 2. Microbubbles' mean size (μm) on different experimental days.

of microbubble suspension in a single vial and the hypothesis that the microbubbles undergo strong changes initially, followed by an eventual equilibrium state. The microbubbles were activated using the procedure mentioned before, and then we performed the attenuation experiments and size measurements simultaneously. All the experiments for a particular day took approximately 120 min and were repeated multiple times from one microbubble vial. On each experimental day, we agitated the microbubble vial gently to redisperse the foam and liquid layer formed inside the vial. To ensure reproducibility, we produced two different batches of lipid solution, and from each batch, we prepared four different vials of microbubble suspension. We performed at least two attenuation experiments and one size measurement from each vial of microbubbles for a specific day of experiment. This made a total of 16 attenuation experiments and eight size measurements for each experimental day. Figure 8 (see the Appendix) offers a schematic of the experiment repetition for this stability study.

RESULTS

Microbubble size and concentration

Figure 2 shows the mean size of microbubbles on different days. The mean sizes were approximately constant at a value of 2.25 μm until the first 13 days, increasing then by more than 10%, reaching a value of 2.5 μm on D20 and D30. The size distributions obtained by optical microscopy of the microbubbles for each day are shown in Figs. 3(a)–3(k). More than 90% of the microbubbles have a diameter between 1 and 5 μm, with polydispersity index (PDI)

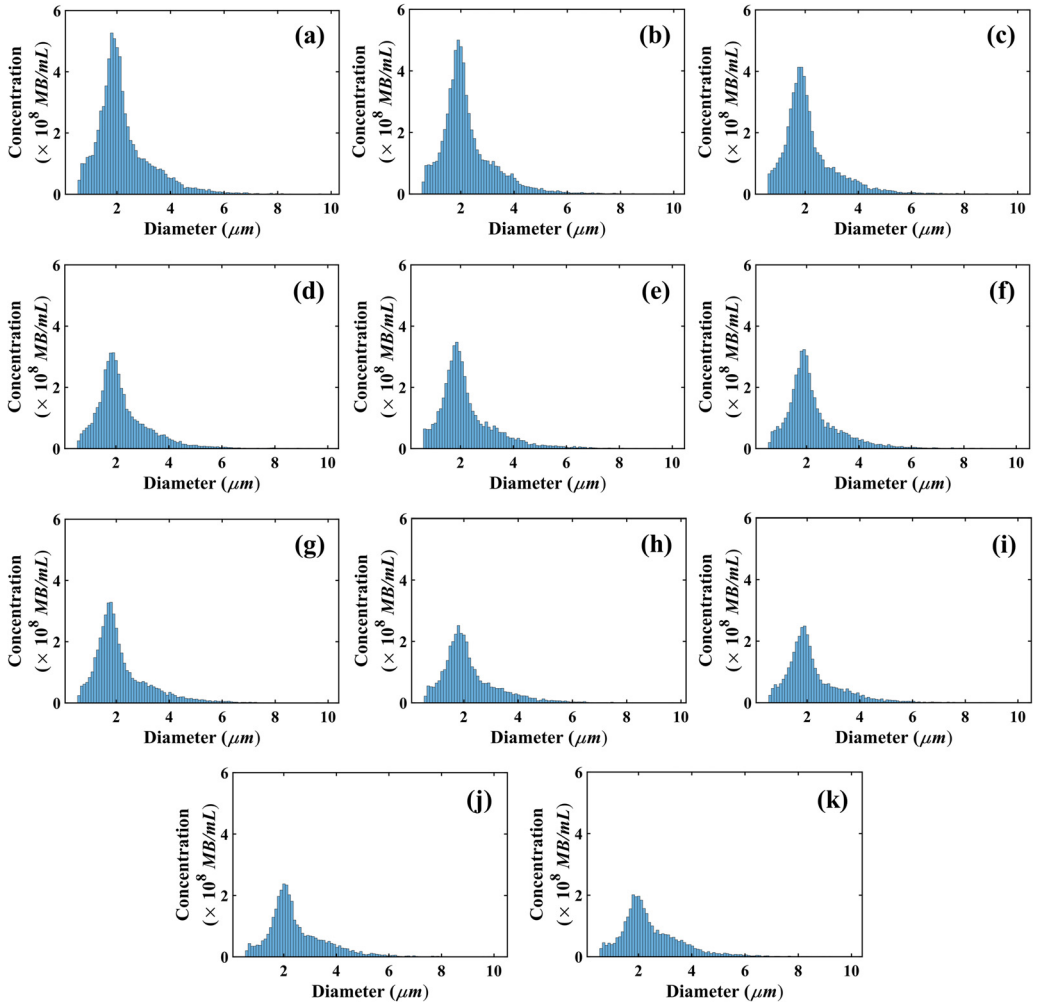

FIG. 3. Size distribution of microbubbles on experimental days of (a) D0T0, (b) D0T6, (c) D1, (d) D2, (e) D3, (f) D4, (g) D7, (h) D10, (i) D13, (j) D20, and (k) D30.

https://doi.org/10.1121/10.0042248

TABLE II. Mean size, total concentration, total volume concentration, and polydispersity index (PDI) of our laboratory-made microbubbles on each day of the experiment.

Day	Mean size (μm)	Total concentration ($\times 10^9$ MB/mL)	Total volume concentration (μL/mL)	Polydispersity index (%)
D0T0	2.24 ± 0.06	7.14 ± 1.12	81.78 ± 19.44	47.00 ± 1.67
D0T6	2.25 ± 0.05	6.55 ± 1.62	74.15 ± 21.62	45.64 ± 2.11
D1	2.17 ± 0.10	5.62 ± 1.15	61.33 ± 12.36	48.66 ± 4.30
D2	2.25 ± 0.16	4.50 ± 0.70	54.33 ± 14.25	47.81 ± 3.71
D3	2.25 ± 0.12	4.86 ± 1.40	58.76 ± 17.86	48.96 ± 3.32
D4	2.25 ± 0.12	4.30 ± 0.95	51.02 ± 12.45	47.91 ± 3.12
D7	2.20 ± 0.07	4.46 ± 0.84	51.29 ± 10.29	49.78 ± 2.40
D10	2.23 ± 0.21	3.53 ± 1.07	40.59 ± 16.25	47.48 ± 2.74
D13	2.23 ± 0.18	3.43 ± 0.53	40.43 ± 5.21	49.46 ± 3.84
D20	2.50 ± 0.08	3.46 ± 0.62	52.47 ± 9.86	46.02 ± 2.48
D30	2.47 ± 0.05	3.29 ± 0.66	50.00 ± 11.00	47.62 ± 4.24

(the ratio between the standard deviation of the size distribution and the mean size) changing between 45.64–49.78% (see Table II). Note that the peak of the size distributions continuously decreased from D0T0 to D30. The mean and the standard deviation of the average size, total concentration, and total volume concentration are given in Table II.

Figure 4(a) plots the concentration density functions from different experimental days. Each histogram dataset (from Fig. 3) was divided by the bin width to obtain the density functions. For clarity, only seven sets—D0T0, D1, D3, D7, D13, D20, and D30—were plotted. The peak decreased continuously. The size distribution shifted toward higher diameters on D20 and D30. Specifically, the density values in the range of 3–5 μm diameters increased, resulting in the higher mean sizes (Fig. 2). The concentration density functions normalized by the total concentration of D0T0, shown in the inset of Fig. 4(a), further illustrate this by showing higher values for the range of 3–5 μm diameters on D20 and D30.

The total concentration of the microbubbles shown in Fig. 4(b) decreased continuously until D13 and then plateaued. The concentration of D30 ($C_{30} = 3.29 \pm 0.66 \times 10^9$ MB/mL) was almost half of the initial time or D0T0 ($C_0 = 7.14 \pm 1.12 \times 10^9$ MB/mL) after activation of the microbubbles. The total concentration $C(t)$ on a specific day (t in hours) was fitted ($R^2 = 0.93$) as

$$C(t) \times 10^{-9} = 3.62 + 3.52e^{-0.0198t}, \tag{8}$$

with an exponential decay constant of 0.0198 h^{-1}. The volume concentration density function plotted over the same period [Fig. 4(c)] shows an increase on D20 and D30. The total volume concentration (see Table II) decreased from the initial value on D0T0 ($V_0 = 81.78 \pm 19.44$ μL/mL) to half its value on D13 ($V_{13} = 40.43 \pm 5.21$ μL/mL). After that, however, on D20 and D30, it increased by 30%, reaching an approximate value of 50 μL/mL. An exponential fit

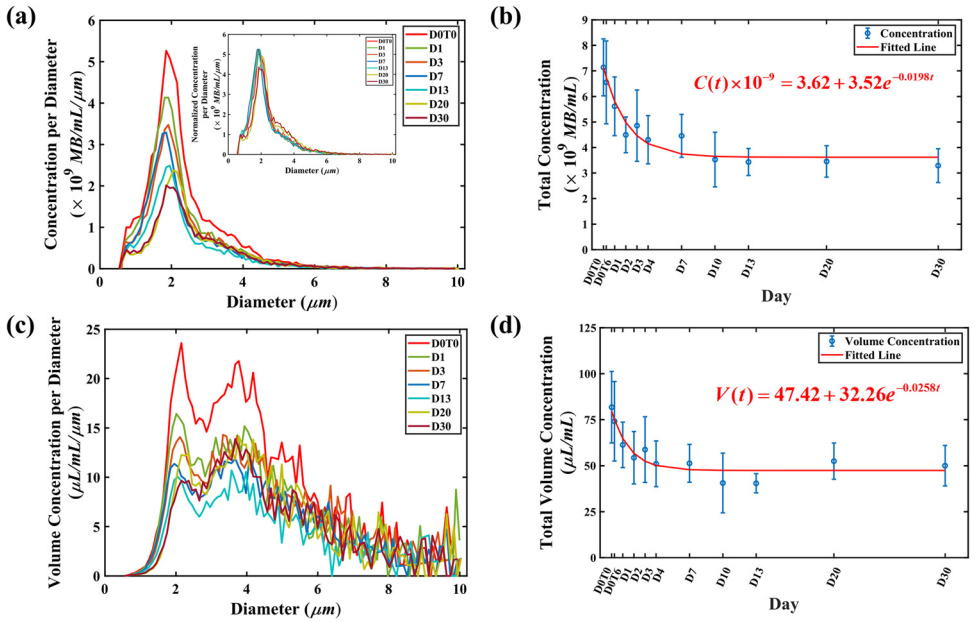

FIG. 4. (a) Size distribution density (inset shows the same data normalized by the total concentration of D0T0), (b) total concentration (MB/mL), (c) volume distribution density, (d) total volume concentration (μL/mL) on different experimental days.

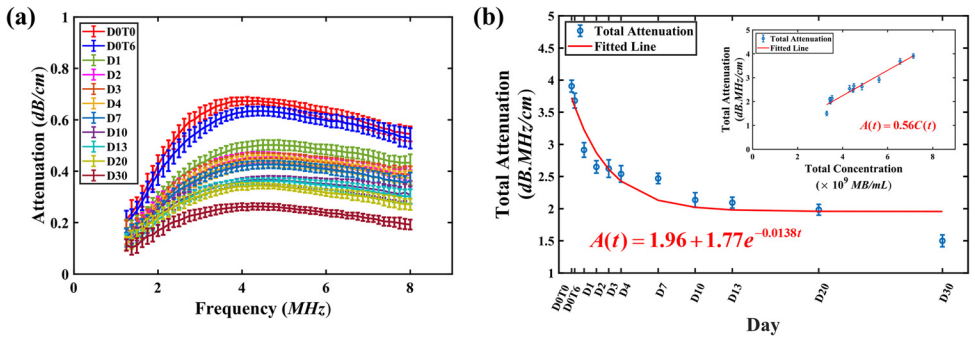

FIG. 5. (a) Attenuation curves on different experimental days, (b) total attenuation vs time (inset shows the total attenuation vs total concentration on different experimental days).

($R^2 = 0.91$) to total volume concentration $V(t)$ with t in hours was plotted in Fig. 4(d),

$$V(t) = 47.42 + 32.26e^{-0.0258t}, \tag{9}$$

with an exponential decay constant of 0.0258 h^{-1}.

Attenuation measurements

Figure 5(a) shows the attenuation coefficients as a function of frequency for each experimental day. The shape of the curves from different days was similar, but the peak value continuously decreased from D0T0 to D30. The attenuation curves were flat with a wide frequency band due to the polydisperse microbubble population, unlike the curves for monodisperse microbubbles with a narrower peak and a tighter frequency band (van Hoeve *et al.*, 2022). The peak frequencies, reported in Table III, are in a range of 4.25–4.75 MHz over the 30 day period. The total attenuation $A(t)$ plotted in Fig. 5(b) shows an exponential decay ($R^2 = 0.89$) with decay constant of 0.0138 h^{-1}, similar to the exponential decay of the total concentration

$$A(t) = 1.96 + 1.77e^{-0.0138t}. \tag{10}$$

Furthermore, we find that the total attenuation plotted vs the total concentration shows the expected linear variation [$A(t) = 0.56C(t)$] with $R^2 = 0.95$ in the inset of Fig. 5(b).

Shell properties estimation

We used the EEM model for predicting the shell properties of the microbubbles using the size distribution and attenuation data for each experimental day. Figure 6 plots the EEM model fits to the experimentally measured attenuation data, showing an excellent match between them. The estimated parameters for shell elasticity (E_0^S), viscosity (κ^S), surface tension (γ_0), and model exponent (α) for EEM and MM models are reported with the confidence intervals in Table IV. Here, the EEM model predicted results similar to the MM model [also seen in our recent study (Paul *et al.*, 2013; Kumar and Sarkar, 2015; 2016; Azami *et al.*, 2022)]. The parameters were almost the same until day 13 and then increased significantly on D20 and D30.

Figures 7(a) and 7(b) show the shell elasticity and shell viscosity of the microbubbles on different experimental days, respectively. The elasticity fluctuated between 1.15–1.36 N/m until day 13. For D20 and D30, the shell elasticity increased by almost 50%, which was 1.93 N/m and 2.01 N/m, respectively. The same trend was observed for the shell viscosity. The viscosity varied between 0.51×10^{-8}–1.83×10^{-8} N.s/m until day 13. Then, it increased nearly 200% for D20 and D30, which were 5.44×10^{-8} N.s/m and 5.59×10^{-8} N.s/m, respectively.

TABLE III. Peak frequency of our laboratory-made microbubbles on each experimental day.

Day	D0T0	D0T6	D1	D2	D3	D4	D7	D10	D13	D20	D30
Peak frequency (MHz)	4.38	4.38	4.63	4.75	4.75	4.75	4.75	4.63	4.50	4.25	4.25

DISCUSSIONS

The overall size distribution, along with its peak, continually decreased for the entire duration [Figs. 3 and 4(a)], indicating initially strong and progressively slower, bubble dissolution also seen by Pouliopoulos *et al.* (2020). Similar to this prior study, we also found an exponentially decreasing microbubble concentration [Fig. 4(b)]. Pouliopoulos *et al.* (2020) used a 1 mg/mL lipid solution with a 9:1 molar ratio mixture of 1,2-distearoyl-sn-glycero-3phosphocholine (DSPC) and 1,2-distearoyl-sn-glycero-3phosphoethanolamine-N-[methoxy(polyethylene glycol) –2000] (DSPE-PEG-2000), in contrast to a 1 mg/mL lipid solution with a 9:1 molar ratio mixture of DPPC and DPPE-PEG-2000 (both slightly shorter chain length) used here. Also, they used 10% v/v (volume/volume) glycerol and 10% v/v 1,2-propanediol (same as propylene glycol) in comparison to 5% v/v glycerol and 15% v/v propylene glycol. They reported an exponential decay constant of 0.02 day^{-1} (0.00083 h^{-1}) compared to 0.0198 h^{-1} found here, which can be explained by the difference in the lipid composition of the shells and the preparation protocol, including different glycerol and the propylene glycol percentage. Note that DSPC microbubbles were shown to be more stable than ones with other lipid shells and therefore can be expected to have a smaller decay rate (Borden and Longo, 2002).

https://doi.org/10.1121/10.0042248

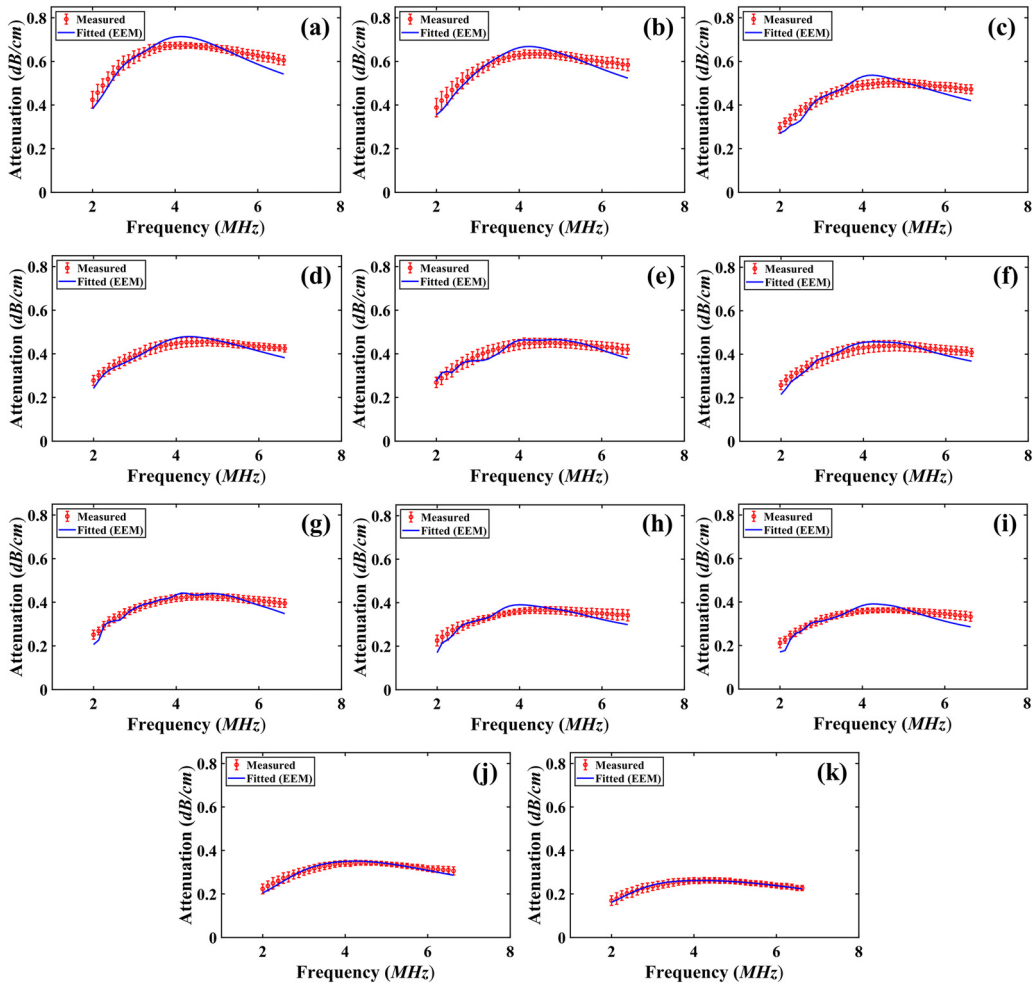

FIG. 6. Exponential elasticity model (EEM) fitted to experimental attenuation data for estimating shell properties on experimental days of (a) D0T0, (b) D0T6, (c) D1, (d) D2, (e) D3, (f) D4, (g) D7, (h) D10, (i) D13, (j) D20, and (k) D30.

The single bubble dissolution in isolation is driven by the residual surface tension of the lipid shell as well as the gradient diffusion of the enclosed PFC gas, limited by the permeability of the shell membrane. With time, as the bubble surface shrinks, the surface tension decreases, slowing down the diffusion. The increased lipid packing also hinders gas diffusion, impeding further dissolution. Previously (Katiyar *et al.*, 2009; Sarkar *et al.*, 2009; Katiyar and Sarkar, 2010), we modeled the diffusion process and arrived at an equation for the changing bubble radius $R(t)$ (Katiyar *et al.*, 2009),

$$\frac{dR}{dt} = \frac{-3L_g k_g}{\left(\frac{k_g}{h_g} + R\right)} \left[\frac{P_0(1-f) + \frac{2\gamma}{R}}{3P_0 + \frac{4\gamma}{R} + 2\frac{d\gamma}{dR}}\right]$$

$$\text{for } \gamma(R) = \gamma_0 + E^s\left[\left(\frac{R}{R_0}\right)^2 - 1\right] > 0,$$

$$\frac{dR}{dt} = \frac{-L_g k_g}{\left(\frac{k_g}{h_g} + R\right)}(1-f) \quad \text{for } \gamma(R) = 0. \tag{11}$$

Here, h_g is permeability of the gas through the shell membrane, k_g is the diffusivity in the surrounding liquid, L_g is the Ostwald coefficient relating dissolved concentration of a gas in the liquid adjacent to the same gas body, and f is the saturation of level of the liquid with the gas. Here, $f=1$ (for PFC filling the vial headspace). Only the nonzero effective surface tension drives the diffusion shrinking the radius. As a result, the surface tension reduces, eventually becoming zero. The equation clearly delineates the effects of the gas solubility (L_g) and diffusivity. The gas permeability through the membrane h_g is expected to decrease with radius due to increased lipid packing. We note that in a vial, the bubbles are at a higher concentration and thereby near each other. It may result in coalescence (controlled by the amount of the PEGylated lipids) as well as Ostwald ripening of larger bubbles at the expense of smaller bubbles, affecting the evolution of bubble concentration seen here. Ostwald ripening has been observed in monodisperse lipid-coated microbubble suspensions (Segers *et al.*, 2016b).

The mean size of the lipid-coated microbubbles remained almost the same until day 13 (Fig. 2). Note that the negligible average size change in the initial period aligns with the study of Pouliopoulos *et al.* (2020), who observed little variation in mean size until 21 days. It also matches with results by Feshitan *et al.* (2009), where they

TABLE IV. Material properties (elasticity, viscosity, surface tension, etc.) using the exponential elasticity model (EEM) and Marmottant model (MM) of our laboratory-made microbubbles on each experimental day. The [· · ·] indicates the confidence intervals.

	Shell elasticity, E_0^S(N/m)		Shell viscosity, κ^S ($\times 10^{-8}$ N.s/m)			
Day	EEM	MM	EEM	MM	Model parameter, α	Surface tension, γ_0 (N/m)
D0T0	1.17	1.18	1.83	1.83	1.39	0.0078
	[1.04–1.30]	[1.05–1.32]	[1.52–2.16]	[1.52–2.17]	[0–7.74]	[0–0.0712]
D0T6	1.15	1.17	1.81	1.81	1.38	0.0077
	[1.04–1.28]	[1.06–1.29]	[1.53–2.12]	[1.53–2.14]	[0–7.71]	[0–0.0707]
D1	1.20	1.21	1.06	1.09	1.44	0.0080
	[1.06–1.35]	[1.07–1.35]	[0.71–1.49]	[0.73–1.52]	[0–8.64]	[0–0.0778]
D2	1.17	1.18	1.44	1.47	1.39	0.0078
	[1.06–1.29]	[1.07–1.30]	[1.17–1.74]	[1.19–1.71]	[0–6.97]	[0–0.0626]
D3	1.36	1.37	0.83	0.88	1.45	0.0091
	[1.24–1.48]	[1.25–1.50]	[0.58–1.17]	[0.60–1.20]	[0–6.44]	[0–0.0617]
D4	1.19	1.21	0.77	0.78	1.38	0.0080
	[1.07–1.33]	[1.08–1.35]	[0.46–1.17]	[0.47–1.18]	[0–7.89]	[0–0.0754]
D7	1.32	1.33	0.51	0.51	1.44	0.0088
	[1.20–1.45]	[1.21–1.46]	[0.20–0.84]	[0.19–0.83]	[0–6.78]	[0–0.0638]
D10	1.23	1.24	0.91	0.93	1.39	0.0082
	[1.08–1.40]	[1.09–1.41]	[0.51–1.39]	[0.53–1.42]	[0–9.12]	[0–0.0909]
D13	1.18	1.18	0.72	0.78	1.40	0.0079
	[1.02–1.36]	[1.03–1.35]	[0.37–1.23]	[0.42–1.27]	[0–9.98]	[0–0.0977]
D20	1.93	1.96	5.44	5.44	1.68	0.0115
	[1.79–2.08]	[1.81–2.10]	[4.99–5.91]	[4.98–5.89]	[0–8.69]	[0–0.0852]
D30	2.01	2.04	5.59	5.59	1.71	0.0118
	[1.94–2.09]	[1.96–2.13]	[5.38–5.83]	[5.39–5.85]	[0–5.06]	[0–0.0458]

showed a stable size until 28 days after size separation of lipid-coated microbubbles using centrifugation. The size increased in D20 and D30. The increase correlated with an increase in size density in the 3–5 μm size range compared to the smaller size microbubbles [Fig. 4(a), inset]. It was also accompanied by an increase in total volume concentration, indicating a net gas volume increase on D20 and D30 [Figs. 4(c) and 4(d)]. Note that the size measurement is limited to microbubbles of size between 0.6–10 μm, but as noted above, changing it led to minimal changes in average size and concentration. Also, the sample is drawn carefully, excluding the foam region (Bergeron and Walstra, 2005) formed by very large bubbles floating up due to buoyancy. The net increase in gas volume in our size measurement can only be explained by gas coming in either from these larger bubbles becoming smaller due to gas diffusion and stirred out of the foam layer into the main dispersion or the smaller bubbles (less than 0.6 μm) losing their gas to bigger bubbles [maybe due to Ostwald ripening for close neighbors of different sizes (Segers *et al.*, 2016b)]. Although the PEGylation of lipids substantially hinders coalescence, there may be some coalescence over time, possibly along with shell buckling and lipid shedding from the microbubbles' shell (Lozano and Longo, 2009). Being interested in extended use of these microbubbles in this study, we stored them at 4 °C following the standard storage protocol. The experiments were performed at room temperature. However, we note that bubble properties depend on temperature as well as other physiological parameters, such as pH, flow, and shear stress. Future investigations of these effects could shed useful information for clinical applications.

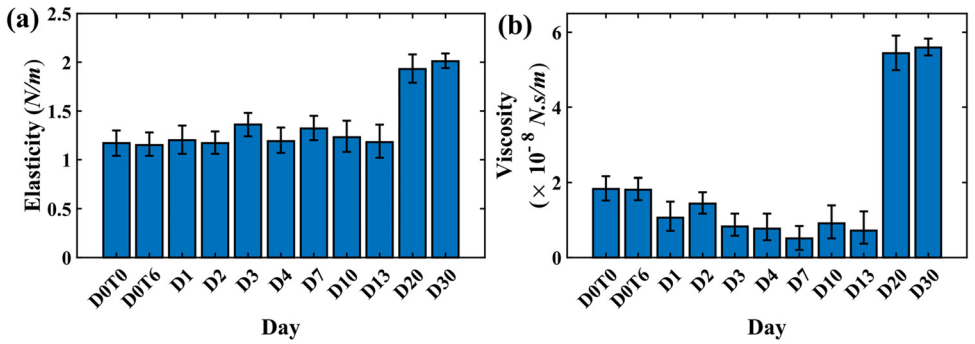

FIG. 7. (a) Shell elasticity and (b) shell viscosity for microbubbles on different experimental days. Error bars correspond to the confidence intervals on each day.

https://doi.org/10.1121/10.0042248

The attenuation coefficient also showed an approximately exponential decrease with time [Fig. 5(b)], similar to the exponential decrease in total concentration [Fig. 4(b)]. Note that attenuation is expected to vary linearly with bubble concentration, as was previously shown by us for Definity microbubbles (Chatterjee *et al.*, 2005). Here, we see that even though the concentration change is occasioned by a natural aging process, the linear relation between the total attenuation and the concentration still holds [Fig. 5(b), inset]. The peak frequency in the attenuation approximately showed an increasing trend until D13 (see Table III), but then slightly decreased on D20 and D30. For a monodisperse suspension of microbubbles, the peak of the attenuation curve occurs at the resonance frequency. However, for a polydisperse suspension as in here, the peak represents a "weighted average frequency" of the suspension where the attenuation is maximum. The attenuation curves [Fig. 5(a)] increasingly broadened over time, making the peak less pronounced and therefore less significant. The decrease in the peak frequency coincided with an increased average size for the last 2 days. The shell elasticity and viscosity obtained using the attenuation data did not vary much until D13 and then recorded a significant increase on D20 and D30 (Fig. 7). Note that the resonance frequency of a microbubble [see Eq. (3)] is inversely related, i.e., a decreasing function of radius and an increasing function of the shell elasticity. We note that with the broad attenuation curves recorded [Fig. 5(a)] for the polydisperse suspension, the inverse method used here to determine the properties, such as elasticity and viscosity, raises some concerns. The properties here were determined using the average size distribution and the average attenuation (Fig. 6) using data from four different vials (see the Appendix). To investigate the robustness of the characterization method used here, we also determined the properties using individual attenuation and size data from each vial. We found that while vial-to-vial variations in attenuation had little effect on the characteristic properties determined, the vial-to-vial variations in size distributions have a significant effect. However, the overall trend noted above in the properties that they increase in D20 and D30, held true even with these variations. The increase in shell elasticities and viscosities could result from maturing and compaction of the shells as they decrease in size by gas diffusion. Note that prior characterization study of lipid-coated monodisperse microbubbles using attenuation by Segers *et al.* (2018) showed similar increase in interfacial elasticity and viscosity with shrinking radii. The same study noted an unusually large value of surface tension quite distinct from prior literature values indicating that different studies using different methods of similar bubbles have often led to different property values.

V. SUMMARY

Here, we studied the laboratory-made lipid-coated microbubbles' long-term size and shell stability. We measured the mean size and total concentration over a 30 day period and performed attenuation experiments on the corresponding days. We used the EEM (as well as the MM) to iteratively estimate the shell parameters (shell elasticity and shell viscosity). We observed that the mean sizes of the microbubbles were almost the same (∼2.25 μm) until day 13, and then they increased slightly (∼2.5 μm) on day 20 and day 30. The total concentration of microbubbles decreased approximately exponentially until day 13 and then saturated. This decrease resulted in an exponential decrease in attenuation coefficients. The total volume concentration also decreased exponentially over time. The shell elasticity and shell viscosity varied a little until day 13. On day 20 and day 30, there were almost 50% and 200% increases in shell elasticity and shell viscosity, respectively. The increase in size and shell properties can be attributed to a number of factors: accretion of bubbles from the foam layer after their shrinkage to a smaller size, coalescence of smaller microbubbles, their Ostwald ripening, and local dynamics, such as lipid shedding and shell buckling. The results established the stability of the microbubbles for more than 13 days, allowing their use for an extended period beyond the current practice of 3–6 h after production in the laboratory or the listed 2–12 h of shelf life of commercial contrast microbubbles. Apart from reduction of wastage, the study further underscores the complex temporal dynamics of contrast microbubbles, which are of crucial importance for their various clinical uses. The experiments were performed at room temperature in a static condition. Future investigations of the effects of physiological conditions, such as body temperature, pH, and flow, could offer useful information for clinical applications.

ACKNOWLEDGMENTS

K.S. and S.M. acknowledge partial support from National Institutes of Health Award No. R01 GM114080. K. S. acknowledges partial support from National Science Foundation Award No. 2037849.

AUTHOR DECLARATIONS

Conflict of Interest

The authors have no conflicts to disclose.

DATA AVAILABILITY

The supporting data of this study will be made available on reasonable request.

APPENDIX: SCHEMATIC OF EXPERIMENTAL INVESTIGATION

Figure 8 shows a schematic of the experiments using samples from different microbubble populations. We prepared two batches of lipid solution and created four different vials of microbubbles from each lipid batch. Then, we performed two attenuation experiments and one size measurement from each vial of microbubble suspension, resulting in a total count of 16 attenuation measurements and eight size distribution measurements.

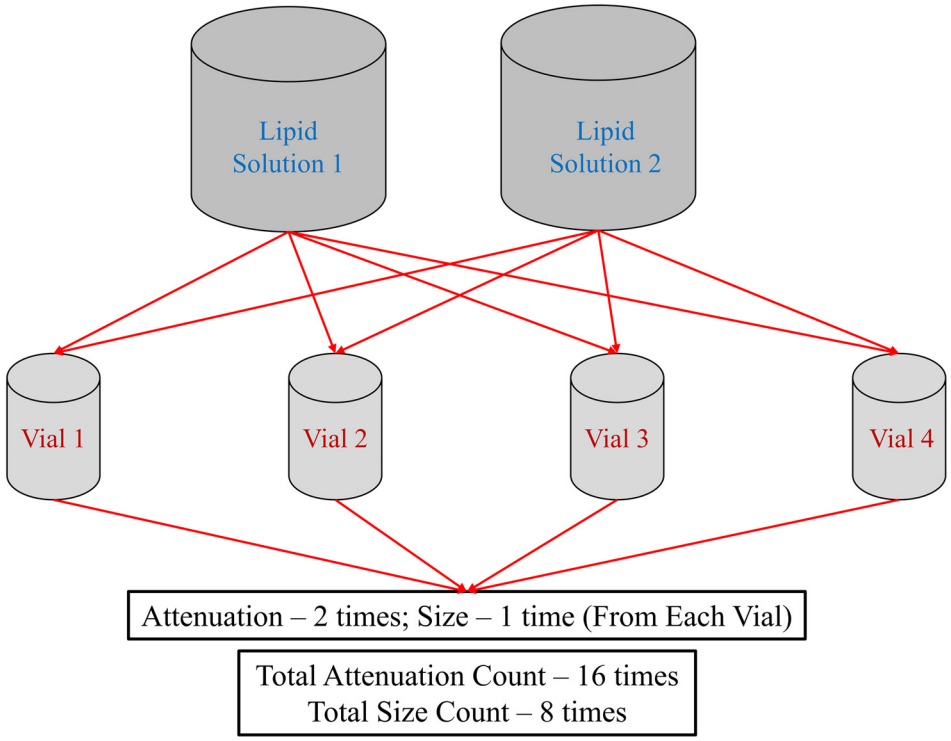

FIG. 8. Schematic of the full experimental observation.

Abbe, E. (**1873**). "Beiträge zur Theorie des Mikroskops und der mikroskopischen Wahrnehmung" ("Contributions to the theory of the microscope and microscopic perception"), Arch. Mikrosk. Anat. **9**, 413–468.

Abbe, E. (**1882**). "The relation of aperture and power in the microscope (continued)," J. R. Microsc. Soc. **2**, 460–473.

Azami, R. H., Aliabouzar, M., Osborn, J., Kumar, K. N., Forsberg, F., Eisenbrey, J. R., Mallik, S., and Sarkar, K. (**2022**). "Material properties, dissolution and time evolution of pegylated lipid-shelled microbubbles: Effects of the polyethylene glycol hydrophilic chain configurations," Ultrasound Med. Biol. **48**, 1720–1732.

Azami, R. H., Forsberg, F., Eisenbrey, J. R., and Sarkar, K. (**2023**). "Ambient pressure sensitivity of the subharmonic response of coated microbubbles: Effects of acoustic excitation parameters," Ultrasound Med. Biol. **49**, 1550–1560.

Azami, R. H., Forsberg, F., Eisenbrey, J. R., and Sarkar, K. (**2024**). "Acoustic response and ambient pressure sensitivity characterization of SonoVue for noninvasive pressure estimation," J. Acoust. Soc. Am. **155**, 2636–2645.

Azami, R. H., Yapar, M., Halder, S., Forsberg, F., Eisenbrey, J. R., and Sarkar, K. (**2025**). "Effects of different gas cores on the ambient pressure sensitivity of the subharmonic response of SonoVue," Ultrasound Med. Biol. **51**, 373–380.

Bergeron, V., and Walstra, P. (**2005**). "Foams," in *Fundamentals Interface Colloid Science, Volume V: Soft Colloids*, edited by J. Lyklema (Elsevier Academic Press, Amsterdam, The Netherlands), Chap. 7, pp. 1–38.

Borden, M. A., and Longo, M. L. (**2002**). "Dissolution behavior of lipid monolayer-coated, air-filled microbubbles: Effect of lipid hydrophobic chain length," Langmuir **18**, 9225–9233.

Chabouh, G., Dollet, B., Quilliet, C., and Coupier, G. (**2021**). "Spherical oscillations of encapsulated microbubbles: Effect of shell compressibility and anisotropy," J. Acoust. Soc. Am. **149**, 1240–1257.

Chatterjee, D., and Sarkar, K. (**2003**). "A Newtonian rheological model for the interface of microbubble contrast agents," Ultrasound Med. Biol. **29**, 1749–1757.

Chatterjee, D., Sarkar, K., Jain, P., and Schreppler, N. E. (**2005**). "On the suitability of broadband attenuation measurement for characterizing contrast microbubbles," Ultrasound Med. Biol. **31**, 781–786.

Church, C. C. (**1995**). "The effects of an elastic solid surface layer on the radial pulsations of gas bubbles," J. Acoust. Soc. Am. **97**, 1510–1521.

Conversano, F., Franchini, R., and Casciaro, S. (**2010**). "Characterization of microbubble contrast agents for echographic imaging through time-scheduled size distribution measurements," Sens. Transducers J. **9**, 21–27.

Cosgrove, D. (**2006**). "Ultrasound contrast agents: An overview," Eur. J. Radiol. **60**, 324–330.

Dash, N., and Tamadapu, G. (**2022a**). "Describing the dynamics of a nonlinear viscoelastic shelled microbubble with an interface energy model," J. Appl. Phys. **132**, 204702.

Dash, N., and Tamadapu, G. (**2022b**). "Radial dynamics of an encapsulated microbubble with interface energy," J. Fluid Mech. **932**, A26.

Dave, J. K., Kulkarni, S. V., Pangaonkar, P. P., Stanczak, M., McDonald, M. E., Cohen, I. S., Mehrotra, P., Savage, M. P., Walinsky, P., Ruggiero, N. J., Fischman, D. L., Ogilby, D., VanWhy, C., Lombardi, M., and Forsberg, F. (**2017**). "Non-invasive intra-cardiac pressure measurements using subharmonic-aided pressure estimation: Proof of concept in humans," Ultrasound Med. Biol. **43**, 2718–2724.

de Jong, N., Emmer, M., Chin, C. T., Bouakaz, A., Mastik, F., Lohse, D., and Versluis, M. (**2007**). "'Compression-only' behavior of phospholipid-coated contrast bubbles," Ultrasound Med. Biol. **33**, 653–656.

Definity (**2001**). "DEFINITY® for diagnostic ultrasound enhancement," https://www.definityimaging.com/ (Last viewed May 16, 2025).

de Jong, N., Hoff, L., Skotland, T., and Bom, N. (**1992**). "Absorption and scatter of encapsulated gas filled microspheres - Theoretical considerations and some measurements," Ultrasonics **30**, 95–103.

Doinikov, A. A., Haac, J. F., and Dayton, P. A. (**2009**). "Modeling of nonlinear viscous stress in encapsulating shells of lipid-coated contrast agent microbubbles," Ultrasonics **49**, 269–275.

Eisenbrey, J. R., Dave, J. K., Halldorsdottir, V. G., Merton, D. A., Miller, C., Gonzalez, J. M., Machado, P., Park, S., Dianis, S., Chalek, C. L., Kim, C. E., Baliff, J. P., Thomenius, K. E., Brown, D. B., Navarro, V., and Forsberg, F. (**2013**). "Chronic liver disease: Noninvasive subharmonic aided pressure estimation of hepatic venous pressure gradient," Radiology **268**, 581–588.

Eisenbrey, J. R., and Forsberg, F. (**2010**). "Contrast-enhanced ultrasound for molecular imaging of angiogenesis," Eur. J. Nucl. Med. Mol. Imaging **37**, 138–146.

Eisenbrey, J. R., Sridharan, A., Liu, J.-B., and Forsberg, F. (**2015**). "Recent experiences and advances in contrast-enhanced subharmonic ultrasound," Biomed. Res. Int. **2015**, 640397.

Esposito, C., Machado, P., McDonald, M. E., Savage, M. P., Fischman, D., Mehrotra, P., Cohen, I. S., Ruggiero, N., Walinsky, P., Vishnevsky, A., Dickie, K., Davis, M., Forsberg, F., and Dave, J. K. (**2023**). "Noninvasive evaluation of cardiac chamber pressures using subharmonic-aided pressure estimation with Definity microbubbles," JACC: Cardiovasc. Imaging **16**, 224–235.

Ferrara, K., Pollard, R., and Borden, M. (**2007**). "Ultrasound microbubble contrast agents: Fundamentals and application to gene and drug delivery," Annu. Rev. Biomed. Eng. **9**, 415–447.

Feshitan, J. A., Chen, C. C., Kwan, J. J., and Borden, M. A. (**2009**). "Microbubble size isolation by differential centrifugation," J. Colloid Interface Sci. **329**, 316–324.
Fix, S. M., Borden, M. A., and Dayton, P. A. (**2015**). "Therapeutic gas delivery via microbubbles and liposomes," J. Control. Release **209**, 139–149.
Forsberg, F., Liu, J.-B., Shi, W. T., Furuse, J., Shimizu, M., and Goldberg, B. B. (**2005**). "In vivo pressure estimation using subharmonic contrast microbubble signals: Proof of concept," IEEE Trans. Ultrason. Ferroelectr. Freq. Control **52**, 581–583.
Forsberg, F., Piccoli, C. W., Merton, D. A., Palazzo, J. J., and Hall, A. L. (**2007**). "Breast lesions: Imaging with contrast-enhanced subharmonic US—Initial experience," Radiology **244**, 718–726.
Frinking, P., Segers, T., Luan, Y., and Tranquart, F. (**2020**). "Three decades of ultrasound contrast agents: A review of the past, present and future improvements," Ultrasound Med. Biol. **46**, 892–908.
Fukutake, N. (**2020**). "A general theory of far-field optical microscopy image formation and resolution limit using double-sided Feynman diagrams," Sci. Rep. **10**, 17644.
Gargouri, F. (**2025**). "Thresholding the maximum entropy - File Exchange - MATLAB Central," https://www.mathworks.com/matlabcentral/fileexchange/35158-thresholding-the-maximum-entropy (Last viewed July 8, 2025).
Gorce, J.-M., Arditi, M., and Schneider, M. (**2000**). "Influence of bubble size distribution on the echogenicity of ultrasound contrast agents: A study of SonoVue™," Investig. Radiol. **35**, 661–671.
Gupta, I., Eisenbrey, J. R., Machado, P., Stanczak, M., Wallace, K., and Forsberg, F. (**2019**). "On factors affecting subharmonic-aided pressure estimation (SHAPE)," Ultrason. Imaging **41**, 35–48.
Gupta, I., Eisenbrey, J. R., Machado, P., Stanczak, M., Wessner, C. E., Shaw, C. M., Gummadi, S., Fenkel, J. M., Tan, A., Miller, C., Parent, J., Schultz, S., Soulen, M. C., Sehgal, C. M., Wallace, K., and Forsberg, F. (**2021**). "Diagnosing portal hypertension with noninvasive subharmonic pressure estimates from a US contrast agent," Radiology **298**, 104–111.
Halder, S., Chaudhury, K., and Mandal, S. (**2025**). "Engineered microbubbles for breast cancer imaging and therapy: From material innovation to clinical translation," ACS Appl. Bio Mater. **8**, 6613–6634.
Halldorsdottir, V. G., Dave, J. K., Leodore, L. M., Eisenbrey, J. R., Park, S., Hall, A. L., Thomenius, K. E., and Forsberg, F. (**2011**). "Subharmonic contrast microbubble signals for noninvasive pressure estimation under static and dynamic flow conditions," Ultrason. Imaging **33**, 153–164.
Hoff, L., Sontum, P. C., and Hovem, J. M. (**2000**). "Oscillations of polymeric microbubbles: Effect of the encapsulating shell," J. Acoust. Soc. Am. **107**, 2272–2280.
Katiyar, A., and Sarkar, K. (**2010**). "Stability analysis of an encapsulated microbubble against gas diffusion," J. Colloid Interface Sci. **343**, 42–47.
Katiyar, A., and Sarkar, K. (**2011**). "Excitation threshold for subharmonic generation from contrast microbubbles," J. Acoust. Soc. Am. **130**, 3137–3147.
Katiyar, A., Sarkar, K., and Jain, P. (**2009**). "Effects of encapsulation elasticity on the stability of an encapsulated microbubble," J. Colloid Interface Sci. **336**, 519–525.
Kumar, K. N., and Sarkar, K. (**2015**). "Effects of ambient hydrostatic pressure on the material properties of the encapsulation of an ultrasound contrast microbubble," J. Acoust. Soc. Am. **138**, 624–634.
Kumar, K. N., and Sarkar, K. (**2016**). "Interfacial rheological properties of contrast microbubble Targestar P as a function of ambient pressure," Ultrasound Med. Biol. **42**, 1010–1017.
Kwan, J. J., and Borden, M. A. (**2010**). "Microbubble dissolution in a multigas environment," Langmuir **26**, 6542–6548.
Lozano, M. M., and Longo, M. L. (**2009**). "Microbubbles coated with disaturated lipids and DSPE-PEG2000: Phase behavior, collapse transitions, and permeability," Langmuir **25**, 3705–3712.
Lumason (**2001**). "LUMASON ® ultrasound enhancing agent," https://lumason.com/ (Last viewed May 16, 2025).
Marmottant, P., Van Der Meer, S., Emmer, M., Versluis, M., De Jong, N., Hilgenfeldt, S., and Lohse, D. (**2005**). "A model for large amplitude oscillations of coated bubbles accounting for buckling and rupture," J. Acoust. Soc. Am. **118**, 3499–3505.
Nio, A. Q. X., Faraci, A., Christensen-Jeffries, K., Raymond, J. L., Monaghan, M. J., Fuster, D., Forsberg, F., Eckersley, R. J., and Lamata, P. (**2020**). "Optimal control of SonoVue microbubbles to estimate hydrostatic pressure," IEEE Trans. Ultrason, Ferroelect, Freq. Contr. **67**, 557–567.
Ogien, J., and Dubois, A. (**2016**). "High-resolution full-field optical coherence microscopy using a broadband light-emitting diode," Opt. Express **24**, 9922–9931.
Optison (**1998**). "Optison™ (Perflutren protein-type A microspheres injectable suspension, USP)," https://www.gehealthcare.com/products/contrast-media/optison (Last viewed May 16, 2025).
Paul, S., Katiyar, A., Sarkar, K., Chatterjee, D., Shi, W. T., and Forsberg, F. (**2010**). "Material characterization of the encapsulation of an ultrasound contrast microbubble and its subharmonic response: Strain-softening interfacial elasticity model," J. Acoust. Soc. Am. **127**, 3846–3857.
Paul, S., Nahire, R., Mallik, S., and Sarkar, K. (**2014**). "Encapsulated microbubbles and echogenic liposomes for contrast ultrasound imaging and targeted drug delivery," Comput. Mech. **53**, 413–435.
Paul, S., Russakow, D., Rodgers, T., Sarkar, K., Cochran, M., and Wheatley, M. A. (**2013**). "Determination of the interfacial rheological properties of a poly(DL-lactic acid)-encapsulated contrast agent using *in vitro* attenuation and scattering," Ultrasound Med. Biol. **39**, 1277–1291.
Pouliopoulos, A. N., Jimenez, D. A., Frank, A., Robertson, A., Zhang, L., Kline-Schoder, A. R., Bhaskar, V., Harpale, M., Caso, E., Papapanou, N., Anderson, R., Li, R., and Konofagou, E. E. (**2020**). "Temporal stability of lipid-shelled microbubbles during acoustically-mediated blood-brain barrier opening," Front. Phys. **8**, 137.
Qin, S., Caskey, C. F., and Ferrara, K. W. (**2009**). "Ultrasound contrast microbubbles in imaging and therapy: Physical principles and engineering," Phys. Med. Biol. **54**, R27–R57.
Sarkar, K. (**2025**). "Dynamics of bubbles and ultrasound: Diagnostic imaging to blood pressure monitoring and tissue engineering," Phys. Rev. Fluids **10**, 030501.
Sarkar, K., Katiyar, A., and Jain, P. (**2009**). "Growth and dissolution of an encapsulated contrast microbubble: Effects of encapsulation permeability," Ultrasound Med. Biol. **35**, 1385–1396.
Sarkar, K., Shi, W. T., Chatterjee, D., and Forsberg, F. (**2005**). "Characterization of ultrasound contrast microbubbles using in vitro experiments and viscous and viscoelastic interface models for encapsulation," J. Acoust. Soc. Am. **118**, 539–550.
Segers, T., de Jong, N., and Versluis, M. (**2016a**). "Uniform scattering and attenuation of acoustically sorted ultrasound contrast agents: Modeling and experiments," J. Acoust. Soc. Am. **140**, 2506–2517.
Segers, T., de Rond, L., de Jong, N., Borden, M., and Versluis, M. (**2016b**). "Stability of monodisperse phospholipid-coated microbubbles formed by flow-focusing at high production rates," Langmuir **32**, 3937–3944.
Segers, T., Gaud, E., Versluis, M., and Frinking, P. (**2018**). "High-precision acoustic measurements of the nonlinear dilatational elasticity of phospholipid coated monodisperse microbubbles," Soft Matter **14**, 9550–9561.
Sennoga, C. A., Mahue, V., Loughran, J., Casey, J., Seddon, J. M., Tang, M., and Eckersley, R. J. (**2010**). "On sizing and counting of microbubbles using optical microscopy," Ultrasound Med. Biol. **36**, 2093–2096.
Sennoga, C. A., Yeh, J. S. M., Alter, J., Stride, E., Nihoyannopoulos, P., Seddon, J. M., Haskard, D. O., Hajnal, J. V., Tang, M.-X., and Eckersley, R. J. (**2012**). "Evaluation of methods for sizing and counting of ultrasound contrast agents," Ultrasound Med. Biol. **38**, 834–845.
Sonazoid (**2006**). "Sonazoid™ An ultrasound contrast agent," https://icus-society.org/wp-content/uploads/2022/02/Sonazoid-Educational-Deck.pdf (Last viewed May 16, 2025).
Stride, E., Segers, T., Lajoinie, G., Cherkaoui, S., Bettinger, T., Versluis, M., and Borden, M. (**2020**). "Microbubble agents: New directions," Ultrasound Med. Biol. **46**, 1326–1343.
van Hoeve, W., de Vargas Serrano, M., te Winkel, L., Forsberg, F., Dave, J. K., Sarkar, K., Wessner, C. E., and Eisenbrey, J. R. (**2022**). "Improved sensitivity of ultrasoundbased subharmonic aided pressure estimation using monodisperse microbubbles," J. Ultrasound Med. **41**, 1781–1789.
Versluis, M., Stride, E., Lajoinie, G., Dollet, B., and Segers, T. (**2020**). "Ultrasound contrast agent modeling: A review," Ultrasound Med. Biol. **46**, 2117–2144.
Wu, J., and Li, R.-K. (**2017**). "Ultrasound-targeted microbubble destruction in gene therapy: A new tool to cure human diseases," Genes Dis. **4**, 64–74.
Xu, Q., Nakajima, M., Ichikawa, S., Nakamura, N., and Shiina, T. (**2008**). "A comparative study of microbubble generation by mechanical agitation and sonication," Innov. Food Sci. Emerg. Technol. **9**, 489–494.
Zhu, Y., Arkin, G., Zeng, W., Huang, Y., Su, L., Guo, F., Ye, J., Wen, G., Xu, J., and Liu, Y. (**2024**). "Ultrasound image-guided cancer gene therapy using iRGD dual-targeted magnetic cationic microbubbles," Biomed. Pharmacother. **172**, 116221.